THE JOURNAL OF PHYSICAL CHEMISTRY B
A JOURNAL OF THE AMERICAN CHEMICAL SOCIETY

pubs.acs.org/JPCB

Article

Harnessing Electron Spin Hyperpolarization in Chromophore–Radical Spin Probes for Subcellular Resolution in Electron Paramagnetic Resonance Imaging: Concept and Feasibility

Vinayak Rane*

Cite This: J. Phys. Chem. B 2022, 126, 2715–2728

Read Online

ACCESS | Metrics & More | Article Recommendations | Supporting Information

ABSTRACT: Obtaining a subcellular resolution for biological samples doped with stable radicals at room temperature (RT) is a long-sought goal in electron paramagnetic resonance imaging (EPRI). The spatial resolution in current EPRI methods is constrained either because of low electron spin polarization at RT or the experimental limitations associated with the field gradients and the radical linewidth. Inspired by the recent demonstration of a large electron spin hyperpolarization in chromophore-nitroxyl spin probe molecules, the present work proposes a novel optically hyperpolarized EPR imaging (OH-EPRI) method, which combines the optical method of two-photon confocal microscopy for hyperpolarization generation and the rapid scan (RS) EPR method for signal detection. An important aspect of OH-EPRI is that it is not limited by the abovementioned restrictions of conventional EPRI since the large hyperpolarization in the spin probes overcomes the poor thermal spin polarization at RT, and the use of two-photon optical excitation of the chromophore naturally generates the required spatial resolution, without the need for any magnetic field gradient. Simulations based on time-dependent Bloch equations, which took into account both the RS field modulation and the hyperpolarization generation by optical means, were performed to examine the feasibility of OH-EPRI. The simulation results revealed that a spatial resolution of up to 2 fL can be achieved in OH-EPRI at RT under in vitro conditions. Notably, the majority of the requirements for an OH-EPRI experiment can be fulfilled by the currently available technologies, thereby paving the way for its easy implementation. Thus, the proposed method could potentially bridge the sensitivity gap between the optical and magnetic imaging techniques.

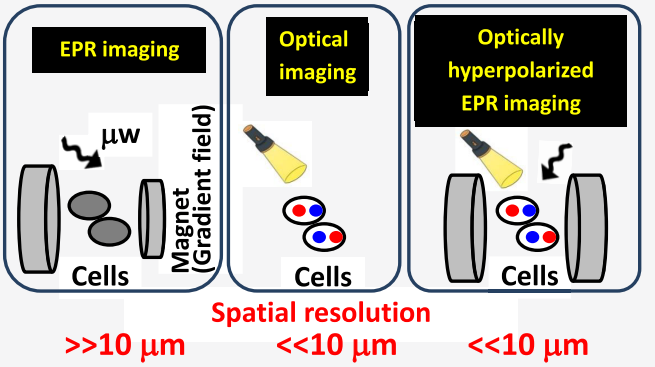

INTRODUCTION

Electron paramagnetic resonance imaging (EPRI) is a powerful magnetic imaging technique that allows three-dimensional (3D) imaging of paramagnetic molecules.[1,2] It has played an important role in a wide range of fields ranging from biomedical,[3] semiconductors,[4] Li-ion batteries,[5] and quantum computing,[6] among others. Especially for biological systems, EPRI has significantly benefitted the field of cancer research, primarily because of its ability to probe molecular O_2 (in tissues, blood, etc.) as well as reactive oxygen species (ROS) such as $O_2^{\bullet-}$, $OH^{\bullet}$, etc. Both of these species, O_2 as well as ROS, are very crucial either for the determination of cancer treatment efficacy or to understand the cancer development and metastasis.[7] However, a significant shortcoming of the EPRI technique is its poor spatial resolution (>10 μm)[8,9] for samples under ambient conditions, which seriously hampers obtaining subcellular information via EPRI. In this regard, it is worth noting that ROS, which is paramagnetic and can be detected via EPR (using suitable spin traps), is often detected by optical techniques primarily because of the latter's ability to provide subcellular information.[10−12] However, optical techniques do not provide a fingerprint of the radical that is being trapped. Furthermore, fluorescent probes, used for their optical detection, are often nonselective, and hence such methods are prone to giving false signals.[8,13,14] Thus, given that EPR is the most direct and unambiguous probe to image paramagnetic molecules, achieving a subcellular resolution in EPRI would greatly benefit to overcome such long-standing issues.

The spatial resolution (Δx) in EPRI for a fixed concentration (~1 mM) of the spin probe depends on a variety of factors. However, the ultimate limit that governs Δx is electron spin polarization (ESP), which is quantified by the parameter $P = (N_\beta - N_\alpha)/(N_\beta + N_\alpha)$, where N_β and N_α are the number of molecules in α and β spin states, respectively. At room temperature (RT) and X-band frequencies, the magnitude of ESP is very small (P_{eq}

Received: December 29, 2021
Revised: February 13, 2022
Published: March 30, 2022

https://doi.org/10.1021/acs.jpcb.1c10920
J. Phys. Chem. B 2022, 126, 2715−2728

$\sim 10^{-3}$), which then ultimately restricts the three-dimensional resolution to more than 1000 μm^3.[15] Apart from the ESP, the ratio of the linewidth of the radical, ΔH, and the magnitude of the field gradient, G_x, are also crucial factors that govern Δx via the equation $\Delta x = \Delta H/G_x$.[16] Because of the direct dependence of Δx on ΔH, spin probes with a very narrow linewidth (i.e., ΔH < 0.1 G) are preferred. However, the most commonly used nitroxyl spin probes have a much larger linewidth ($\Delta H \sim 1$ G). Furthermore, since finite limits exist on the maximum G_x that can be applied, Δx cannot be reduced for unlabeled nitroxyls by simply increasing G_x.[17,18] Even, the use of Fourier transform (FT)-based methods has not been helpful for the unlabeled nitroxides due to their short spin−spin relaxation time, T_{2e}. Hence, isotopically labeled (^{15}N,^{2}D)-nitroxyls are preferred,[19,20] which makes the whole experiment quite expensive and synthetically demanding.

To this end, it is worth mentioning the methodology of optically generated electron spin hyperpolarization (ESH),[21−30] which involves the generation of a transient ESP, P_{Pol}, that is significantly larger than the thermal ESP, P_{eq}. The ESH is generated in the radical through optical excitation of a suitable chromophore that is tethered to the free radical. Notably, in recent times, an enormous ESH of about 500 times the thermal ESP at RT has been demonstrated in an anthraquinone-nitroxide-based chromophore−radical (CR) adduct molecule.[31] Such a large ESH has great potential to overcome the poor ESP at RT, which severely restricts the value of Δx in EPRI. In addition, a notable aspect of optically generated ESH is that it gives an optical handle to induce an observable EPR signal. Consequently, the optical excitation itself can result in the spatial encoding of the radical in an imaging experiment, thereby completely removing the requirement of the field gradients in the EPRI method. Furthermore, since only the optically excited region will be observed, even the linewidths of the spin probe would not be a governing factor for Δx. Thus, in principle, a hyperpolarization-based imaging method could overcome all of the limitations associated with unlabeled nitroxides and hence could result in a high resolution in EPRI experiments. This is the essential idea that is proposed in this current work.

In this work, an EPR imaging method based on a hyperpolarized EPR signal, termed optically hyperpolarized-EPRI (OH-EPRI), is proposed, and the conditions for its feasibility and its potential to achieve a subcellular resolution are examined. This manuscript is organized as follows: The first section presents the proposed idea of OH-EPRI and the subsequent sections examine its feasibility. Specifically, numerical simulations based on time-dependent Bloch equations (TDBE), which account for the ESH generation, are carried out for the anthraquinone-based CR molecules. It is worth pointing out that the CR molecules are covalently linked (Chart S1), which makes the hyperpolarization generation independent of the relative translational diffusion of the C and R moieties. Lastly, the optical excitation efficiency of CR adduct molecules necessary to achieve a subcellular resolution in OH-EPRI experiments is examined. The central finding of this work is that it should be possible to achieve a spatial resolution of up to 2 fL (2 μm^3) in an in vitro imaging experiment at X-band and RT, using a typical probe concentration of 1 mM.[32]

Optically Hyperpolarized-EPRI (OH-EPRI): The Concept. The basic idea on which OH-EPRI rests is the generation of a hyperpolarized EPR signal in a spatially defined manner by optical means, followed by its detection via EPR so that spatial distribution of the spin probes, i.e., the CR molecule can be obtained. Since the optical excitation itself provides a means for spatial encoding, two-dimensional (2D) imaging can be performed by simply scanning the excitation source along the surface of the sample and recording the resulting hyperpolarized EPR spectrum from each pixel. However, such a method cannot provide a 3D resolution since all of the molecules along the path of the beam would get excited, and thus the spatial encoding cannot be attained along this dimension. To this end, some of the ideas from the optical 3D imaging techniques can be utilized, where the resolution is similarly governed by the light source. Notably, the method of two-photon (2P) confocal imaging (2PCI) deserves special mention. In the 2PCI technique, a high 3D resolution is achieved by tight focusing of the excitation light (typically a femtosecond (fs) laser), which causes 2P excitation of a desired molecule. Since the 2P absorption cross section of a molecule requires a high photon flux, the 2P absorption is strongly localized at the focal volume of the laser, thereby providing a high 3D spatial contrast (<μm^3).[33] Thus, it is precisely this aspect of 2P excitation of 2PCI that can be adapted to OH-EPRI to perform a 3D magnetic imaging experiment.

To this end, the conceptual framework of 2PCI microscopy can be potentially extended to the OH-EPRI method (i) using an excitation source (i.e., the laser) that causes 2P excitation of the CR spin probe and (ii) merging the confocal excitation setup with the EPR spectrometer. Importantly, the second aspect involves tight focusing of the laser at the sample. In 2PCI setups, this is primarily achieved using a large numerical aperture lens and placing it as close as possible to the sample.[33] This is, however, difficult to achieve in a typical cavity-based (X-band) EPR spectrometers due to the space restrictions imposed by closed cavity resonators. Thus, an open cavity like planar microresonators[34,35] is needed.

Thus, the basic protocol of the OH-EPRI experiment can be summarized as follows (Figure 1): Illumination of the sample

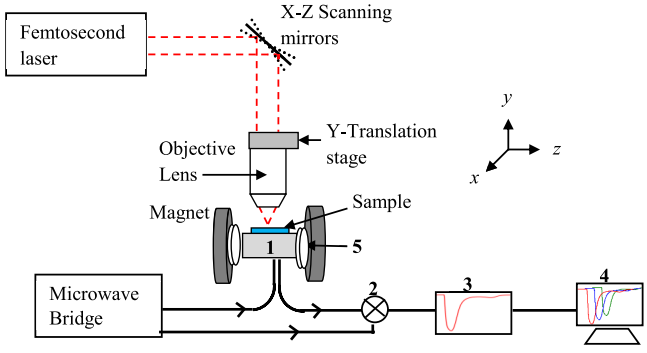

Figure 1. Schematic of the setup for the proposed OH-EPRI experiment. The $X-Z$ scanning mirrors and the Y-translation stage enable the 3D scanning of the laser over the sample. The numbered components are 1: microresonator; 2: balanced mixer detector; 3: digitizer with a continuous data transfer mode so that the data can be transferred to an external storage device while the acquisition is going (Appendix SIV); 4: external storage device (like PC), and 5: field modulation coils.

placed on a planar microresonator of a conventional EPR spectrometer, with a tightly focused laser. This should lead to photoexcitation and subsequent hyperpolarization generation in only those spin probe molecules that are present within the focal volume. The resulting time-resolved EPR (TREPR) signal can be stored and processed via a fast digitizer, which would, in turn, give a measure of the amount of the spin probe in the irradiated

https://doi.org/10.1021/acs.jpcb.1c10920
J. Phys. Chem. B 2022, 126, 2715−2728

volume element. The laser can then be spatially scanned (via the scanning mirrors and the *Y*-translation stage) like 2PCI microscopy to generate the 3D spatial profile of the spin probe. As is evident, no magnetic field gradients are needed for spatially encoding the EPR signal.

MATERIALS AND METHODS

ANCOOT and Anq1Pr were synthesized as per the earlier procedure.[31,36] Steady-state and time-resolved EPR spectra were recorded in a laboratory-built X-band EPR spectrometer.[37] For the time-resolved EPR, the excitation source was the third harmonic of an Nd:YAG laser (Quantel model: YG-981C, wavelength: 355 nm, repetition rate: 15 Hz, energy output: ∼1.5 mJ per pulse, energy at the sample: ∼0.9 mJ per pulse). Because of the strong spin-polarized EPR signals and the laser-induced sample heating, the laser energy was restricted to this low value. The absorbance of all of the solutions at the excitation wavelength was less than 1. The samples were made in quartz tubes (O.D.: 4 mm, I.D.: ∼3 mm, Wilmad Glass) and degassed by three cycles of freeze−pump−thaw under a vacuum of 10^{-5} mbar.

The laser energy absorbed by the sample, which determines the number of excited state molecules, was measured as follows: A slit was inserted in front of the laser entry hole of the microwave (μw) cavity (Figure 2). The best alignment of the

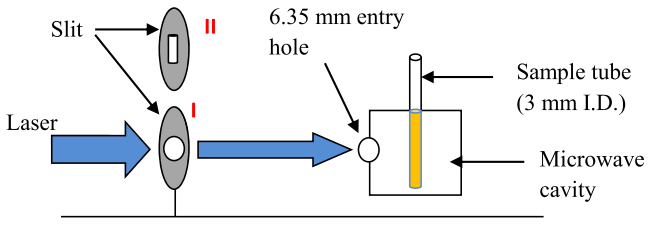

Figure 2. Arrangement of the slit in front of the microwave cavity for measurement of the laser energy.

slit, the hole of the cavity, and the EPR sample were achieved by maximizing the transient EPR signal of Anq1PR. This ensured a collinear arrangement of the slit hole and the cavity hole, and the energy of the laser measured after the slit was taken to be the energy incident on the sample.

Two types of slits were tried:

(i) A circular slit (I) of a diameter 6.35 mm. This diameter was the same as that of the laser entry hole in the front surface of the cavity.

(ii) A rectangular slit (II) of 6.35 × 3.00 mm^2. Here, 6.35 mm was the same as the diameter of the laser entry hole and 3.00 mm was the I.D. of the EPR sample tube.

Slit I was easier to align with the sample tube and the cavity hole. However, the energy measured after it was more than what the sample received since the tube I.D. was 3 mm. So a geometrical correction factor was applied (as mentioned below). Slit II was of the exact dimension as the sample tube and ideally needed no correction. However, its alignment needed a very critical positioning of the sample tube and the slit. Additionally, even after achieving the best possible alignment, it was observed that the signal height was reduced by ∼1.4 times after insertion of the slit. Ideally, no reduction was expected for a perfect alignment, as the dimensions of slit II matched with those of the sample tube. In view of this, the experiments were performed with only silt I without sacrificing the signal intensity but by applying a suitable correction factor for the energy actually reaching the sample. The correction factor (X^{CF}) for the circular slit was found as follows.

X^{CF} is the fractional energy of the laser beam, passing through the slit I, which irradiated the sample kept in the 3.0 mm O.D. tube. To estimate X^{CF}, I first measured the laser energy after (i) both slits I and II in a collinear geometry and (ii) slit I only. This showed that about 64% of the energy after slit I passed through slit II. Since slit II resembles the tube dimensions, the correction factor was assumed to be 0.64.

Next, the abovementioned correction was verified by a geometrical estimation of X^{CF}. In this regard, I assumed a Gaussian intensity profile, $I(x,y)$, for the laser beam (6.4 mm diameter) whose intensity reduces to $1/e^2$ of its value at the center (I_0) of the laser beam. This could be represented as

$$I^{\text{Laser}}(x, y) = I_0\, e^{(-2(x^2+y^2))/3.2^2} \tag{1}$$

The correction factor amounts to estimating the fractional energy of the laser beam present within the tube area, i.e., PQRS in the figure below.

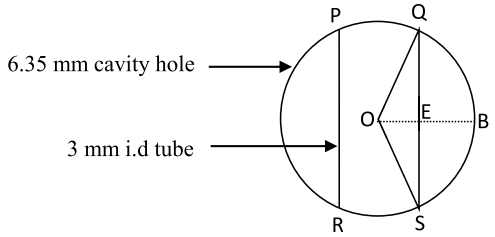

where OE = 1.5 mm (assuming that the tube axis aligns exactly with the center of the cavity hole) and OB = 3.2 mm (half of the cavity hole diameter).

Based on the dimensions of the slit and the tube I.D., the energy after the circular slit (E^{slit}) and that reaching the sample tube (E^{tube}) can be represented as

$$E^{\text{Slit}} = \int_0^{x=3.18} \int_0^{y=\sqrt{r^2-x^2}} I^{\text{Laser}}(x, y)\, dx\, dy$$

$$E^{\text{tube}} = \int_0^{x=1.5} \int_0^{y=\sqrt{r^2-x^2}} I^{\text{Laser}}(x, y)\, dx\, dy \tag{2}$$

The abovementioned integrals were evaluated numerically. The correction factor was given by $E^{\text{tube}}/E^{\text{slit}}$ and was found to be 0.72. This is consistent with the abovementioned experimentally determined correction factor of 0.64. Thus, I used a correction factor of 0.64 in all of the experiments.

The EPR time profiles were collected after locking the magnetic field to the desired position, using a magnetic field-microwave frequency interlock. Each transient was collected alternately at "on-resonance" and "off-resonance" by step modulating the magnetic field by 5 G at 15 Hz (fixed by the laser repetition rate). Normally, an AC-coupled amplifier blocks the steady-state EPR signal due to the Boltzmann population difference. But our experiments, which involve modulating the magnetic field synchronously with the laser repetition rate, ensured that the Boltzmann signal passed through the AC-coupled preamplifier and was recorded by a transient recorder. The true EPR signal was obtained by subtracting the off-resonance curve from the on-resonance curve. This subtraction also removes any nonresonant artifact that rides on the observed microwave signal when the laser pulse enters the microwave cavity.

https://doi.org/10.1021/acs.jpcb.1c10920
J. Phys. Chem. B 2022, 126, 2715−2728

The hyperpolarization time profiles of rapid scan (RS) EPR spectra were simulated by coupling the time-dependent Bloch equations for the rapid scan modulation with suitable hyperpolarization generating terms. To account for the rapid scan conditions, a sinusoidal field modulation was used.[38] The phase of the modulation was adjusted such that the resonance line appears at the center of the scan, where the scan rate is the maximum. To account for the hyperpolarization generation, a strategy similar to our earlier work was followed. Here, the hyperpolarization generation is represented by two terms, corresponding to quenching of the singlet (S^1−R) and the triplet (T^1−R) state of the chromophore in the linked CR molecule.[37]

$$\frac{d[S^0-R_S^*]}{dt} = P_S k_{qs}[S^1-R] \tag{3}$$

$$\frac{d[S^0-R_T^*]}{dt} = P_T k_{qt}[T^1-R] \tag{4}$$

Where $S^0-R_S^*$ and $S^0-R_T^*$ are the absorptive and emissive spin-polarized molecules, k_{qs} and k_{qt} are the singlet state and triplet state quenching rate constants of the chromophore, respectively, and P_S and P_T are the magnitude of the absorptive and emissive hyperpolarization generated via radical triplet pair mechanism (RTPM), respectively. Thus, the resulting time-dependent Bloch equations in the rotating frame are given by

$$\frac{dM_x}{dt} = \frac{-M_x}{T_{2e}} + [\Delta\omega + 0.5|\gamma|B_m \cos(\omega_m t)]M_y$$

$$\frac{dM_y}{dt} = \frac{-M_y}{T_{2e}} - [\Delta\omega + 0.5|\gamma|B_m \cos(\omega_m t)]M_x + |\gamma|B_1 M_z$$

$$\frac{dM_z}{dt} = \frac{M_0 - M_z}{T_{1e}} - |\gamma|B_1 M_z + P_S k_{qs}[S^1 - R] - P_T k_{qt}[T^1 - R] \tag{5}$$

where $\Delta\omega = \omega - \omega_0$ is the offset of a spin packet from the center of the scan in angular frequency units, $|\gamma|$ is the magnitude of the electron gyromagnetic ratio, $\omega_m = 2\pi f_m$ is the angular scan frequency, B_1 is the microwave magnetic field, T_{1e} is the spin−lattice relaxation time, and $[S^1-R]$ and $[T^1-R]$ are the concentration of the singlet state and triplet state of the chromophore in the presence of a radical, which were obtained, in turn, by solving a corresponding kinetic scheme (Scheme 1) for the spin probe molecule.

The various processes in the abovementioned scheme along with their corresponding rate constants are summarized below

$S^1-R \rightarrow S^0-R$ radiative decay (k_{fl})

Scheme 1. Kinetic Scheme of the RTPM Pathway

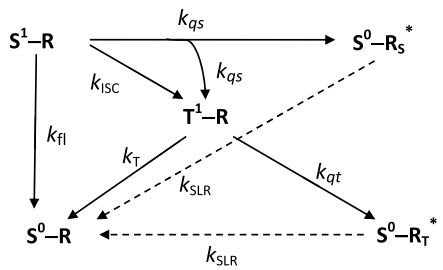

$S^1-R \rightarrow T^1-R$ S^1-R intersystem crossing (k_{ISC})

$S^1-R \rightarrow T^1-R + S^0-R_S^*$

S^1-R quenching by radical via EISC (k_{qs})

$T^1-R \rightarrow S^0-R_T^*$

T^1-R quenching by radical via EISC (k_{qt})

$T^1-R \rightarrow S^0-R$ T^1-R intersystem crossing (k_T)

The spin−lattice relaxation process, k_{SLR}, brings the polarized radicals, $S^0-R_S^*$ and $S^0-R_T^*$, to Boltzmann distribution. This process, shown in dotted lines in the abovementioned scheme, is not used in the kinetic scheme since it is included in the Bloch equation (eq 5). The terms in eqs 3 and 4 were added to the z-component of the magnetization. The resulting Bloch equations in the rotating frame are given by eq 5. These were numerically solved by the fourth order Runge−Kutta method. Simulations were performed for the case of $\Delta\omega = 0$, i.e., a zero offset of the spin packet from the center of the scan. For the initial conditions, the equilibrium steady-state values of the magnetization corresponding to a magnetic field at the start of the scan ($B_0 = B_{res} + B_m/2$) were used.

The values of the various kinetic parameters were $k_{qs} = 2.4 \times 10^9\ s^{-1}$, $k_{qt} = 10^8\ s^{-1}$, $k_{ISC} = 2.5 \times 10^{12}\ s^{-1}$, $k_T = 5 \times 10^6\ s^{-1}$, and $k^{fl} = 0\ s^{-1}$, obtained from the earlier optical/TREPR studies of Anq1Pr.[31] Since the CR molecules are covalently linked, the relative translational diffusion of the C and R moieties can be safely excluded. Moreover, earlier studies have established that the hyperpolarization generation in the Anq1Pr molecule is purely intramolecular. Hence, the abovementioned kinetic scheme did not consider any intermolecular processes.

It is worth pointing here that the true spin states of the linked chromophore−radical molecule that participate in hyperpolarization generation via the RTPM process are the doublet (D_1) and quartet spin states (Q_1).[39] In fact, in the literature, a more rigorous hyperpolarized Bloch equation scheme that incorporates the doublet and quartet states (termed D_1-Q_1 scheme) has also been proposed.[40] However, the D_1-Q_1 scheme is more suitable for those C−R molecules that show the signature of D_1 and Q_1 states in the TREPR spectra. In the case of Anq1Pr, the D_1 and Q_1 states are not seen in the TREPR spectra (even at the earliest gate time of 100 ns) due to their very short lifetime (<10 ns). For such systems where the quenching process is efficient, it was found that the simplified scheme may be considered as a good approximation of the more realistic D_1-Q_1 scheme.[40] Moreover, the D_1-Q_1 scheme also needs knowledge of extra parameters such as the D_1-Q_1 conversion rate constant, whose value is not accessible. Thus, I followed the simplified Bloch equation scheme involving S_1-R and T_1-R states.

RESULTS

Given that the cellular volumes (V_m) are typically of the order of 100−10 000 μm^3 (for example, the widely used HeLa cells have $V_m \sim 2600\ \mu m^3$),[41] the present work strives for achieving spatial resolutions of about 1 μm^3 in the OH-EPRI method. Furthermore, noting that the typical concentration of the spin probes used in imaging experiments is ~1 mM,[19,20] which results in $\sim 10^6$ molecules in the 1 μm^3 volume, the EPR sensitivity, S_{min}, which is defined as the minimum number of

https://doi.org/10.1021/acs.jpcb.1c10920
J. Phys. Chem. B 2022, 126, 2715−2728

spins that can be detected with a signal-to-noise ratio (SNR) of unity per Gauss of linewidth (and normalized with respect to the square root of seconds of the measuring time),[42] also needs to be of this order (i.e., $S_{min} \sim 10^6$ spins·G^{-1}·Hz$^{-1/2}$). To this end, the sensitivity of a typical TREPR spectrometer operating at the X-band frequency at RT was examined since typical spin-polarization measurements are performed in such spectrometers. An Anq1Pr molecule was used as a standard molecule due to its large ESH generation[31] (Chart S1). To differentiate the sensitivity that can be obtained from a hyperpolarized signal, the conventional sensitivity that refers to thermal spin polarization is termed thermal sensitivity.

Figure 3 shows the transient profile of the low-field hyperfine line of the Anq1Pr molecule in benzene, after 355 nm laser

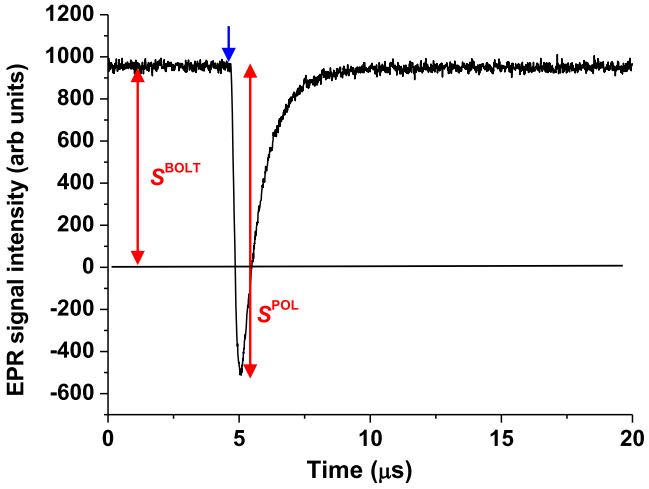

Figure 3. Time profile of the EPR signal recorded at the exact resonance position of the low-field hyperfine line after a 355 nm laser pulse. The time of the laser pulse is marked by a blue arrow. The two red double-headed arrows show the Boltzmann and the spin-polarized signal height. Laser energy = 0.93 mJ per pulse (15 Hz frequency), pulse width ~6 ns, no. of averages = 3, total acquisition time = 0.2 s, temperature = 295 K, concentration of the molecule = 2 mM, volume of solution in the cavity (governs the Boltzmann signal) = 0.160 cm^3, photoexcitation volume = 0.045 cm^3, and absorbance at 355 nm = 0.354.

excitation at RT. The signal height before the laser represents the Boltzmann signal (S^{Bolt}), while the dip of the signal immediately after the laser pulse represents the polarized signal, S^{Pol}. The standard deviation of the noise, σ_{noise}, was determined to be 14.8 (using the first 400 data points), which resulted in the SNR of 64.9 and 99.6 for the Boltzmann and polarized signal, respectively. Based on the concentration and the volume of the sample in the cavity, the total number of spins contributing to S^{Bolt} was evaluated to be $N^{Bolt} = 1.9 \times 10^{17}$. Similarly, using the laser energy falling on the sample and the absorbance of the anthraquinone moiety at 355 nm, the number of spins contributing to S^{Pol} was estimated to be $N^{pol} = 9.5 \times 10^{14}$. Next, the sensitivity of the TREPR spectrometer, for the Boltzmann molecules, S_{min}^{Bolt}, and the polarized molecules, S_{min}^{Pol}, at 1 mW of observing microwave power was obtained by[42,109]

$$S_{min}^{Bolt/Pol} = \frac{N^{Bolt/Pol} \times \sqrt{t_{acq}}}{SNR^{Bolt/Pol} \times \Delta H_{pp}} \quad (6)$$

where ΔH_{pp} is the peak-to-peak first-derivative linewidth (~1 G for Anq1Pr) and t_{acq} is the total acquisition time of the experiment (0.2 s).

Using eq 6, S_{min} values for the Boltzmann molecules and the polarized molecules were estimated to be $(1.2 \pm 0.1) \times 10^{15}$ and $(4.0 \pm 0.4) \times 10^{12}$ spins·G^{-1}·Hz$^{-1/2}$, respectively. Thus, it is evident that in spite of improvement in the sensitivity by over 2 orders of magnitude by the ESH, S_{min}^{Pol} is about 6 orders of magnitude smaller than the desired sensitivity of 10^6 spins needed for subcellular resolution. In fact, even the Boltzmann sensitivity obtained via the abovementioned TREPR detection is very poor compared to that of a typical X-band continuous wave (CW)EPR spectrometer ($S_{min}^{Bolt} \sim 10^{11}-10^{12}$ spins·G^{-1}·Hz$^{-1/2}$).[43] Furthermore, the TREPR detection also has a drawback that the TREPR time profile does not give any information about the spectrum of the paramagnetic species unless the fixed Zeeman field is scanned. Such a detection scheme would make the whole imaging experiment quite time-consuming. Thus, for the present proposed method of OH-EPRI, where the sensitivity, the time resolution, and the identity of the species are highly desired, the conventional TREPR detection scheme would only be of restricted use.

In this regard, it is worth considering the method of rapid scan (RS) EPR, which can not only achieve an enhanced sensitivity and a fast time resolution but also possesses the capability of providing the entire EPR spectrum of the radical species.[44] In RSEPR, the Zeeman field B_0 is scanned very fast through the resonance position of an EPR line, such that the dwell time of the magnetic field is shorter than the spin relaxation times of the paramagnetic molecule.[44,45] This results in two main advantages: (i) multiple scans can be averaged in the same acquisition time as that of a single CWEPR scan (time averaging) and (ii) a much higher microwave power can be applied compared to that in TR/CWEPR (without causing any sample saturation). Depending on the sample, these two aspects result in an improvement of the SNR by a factor of 10−250 times compared to that of the CWEPR method.[44] Notably, for a nitroxide-based radical, an improvement by a factor of 40 has been demonstrated at RT,[46] which clearly points toward its benefits for the proposed hyperpolarized imaging method. However, to date, RSEPR has never been used to examine spin-hyperpolarized systems. Thus, the spin dynamics under RS conditions remains unknown and hence it is difficult to predict a specific enhancement in sensitivity via hyperpolarization in an RSEPR experiment.

To this end, I performed numerical simulations based on the time-dependent Bloch equations (TDBE), which have been very successful in rationalizing the spin dynamics under the rapid scan conditions[47−49] as well as for the hyperpolarization generation.[30,39,50−55] The Bloch equations, as applicable for the RSEPR, have terms that account for the fast scan of the Zeeman magnetic field (characterized by the scan frequency, f_m, and the peak-to-peak scan amplitude B_m).[38] The ESH generation via the radical triplet pair mechanism (RTPM) (or the reverse quartet mechanism[39] for the linked C−R molecules) is included by adding two extra terms in the Bloch equations,[31,36,56] which account for the generation of hyperpolarization by singlet and triplet state quenching of the chromophore. In the present case, I adopted a similar strategy and added those extra terms in the RSEPR Bloch equations, eq 5 (see the Materials and Methods section).

First, a perdeuterated ^{15}N-TEMPONE (PDT, Chart S1) molecule was examined for hyperpolarization generation under RSEPR conditions primarily because its RSEPR has been

https://doi.org/10.1021/acs.jpcb.1c10920
J. Phys. Chem. B 2022, 126, 2715−2728

extensively studied earlier and hence can act as a reference for the dark conditions.[47] The laser pulse was fixed at the start of the field cycle scan and an emissive hyperpolarization magnitude of 10 times the thermal electron polarization was considered. Figure 4 shows an RSEPR time profile in the absence and

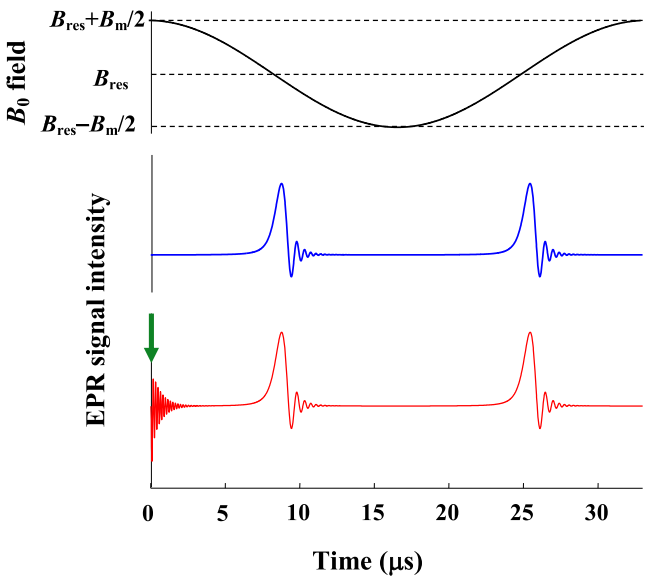

Figure 4. Simulation of the RSEPR time profile of the PDT molecule based on Bloch equations under dark (middle panel, blue curve) and light (red curve) conditions for one full cycle of the field scan. Simulation parameters: blue trace: f_m = 30 kHz, B_m = 4.4 G, T_1 = 0.79 μs, T_2 = 0.61 μs (same a ref 47), microwave power = 1 mW, and P_T = 0; red trace: P_T/P_{eq} = −10 (for other optical parameters see the Materials and Methods). The top panel shows the time profile of the Zeeman (B_0) field during one cycle of the field scan. The green arrow marks the timing of the laser pulse for the red trace. The scale of the vertical axis is the same for the middle and bottom panels.

presence of light for one complete cycle of the field scan (f_m = 30 kHz, B_m = 4.4 G). The simulation for the dark condition reproduced all of the essential features of the earlier experimental/simulated RSEPR profile of PDT in 80% ethanol−water.[47] Notably, the wiggles, which are the characteristic of the RSEPR experiments, were clearly evident toward the falling trail of the resonance EPR signal. However, in the presence of laser irradiation, a strong oscillatory signal was seen at the initial time, which was not present under dark conditions. Furthermore, no enhancement due to hyperpolarization was seen in the resonance signals with respect to that of dark conditions.

This behavior can be rationalized by noting that the timing of the laser pulse in the abovementioned simulations actually correlates with an off-resonance position of the Zeeman field, i.e., at t = 0, $B_0 = B_{res} + B_m/2$ (Figure 4, top panel), where B_{res} is the Zeeman field corresponding to the exact resonance position of the EPR line. For such off-resonance positions, the Bloch equations naturally predict transient oscillations (termed Torrey oscillation)[52,57] for any disturbance of the equilibrium condition (such as the creation of hyperpolarization in the present case). This was confirmed by running the simulations at a fixed (f_m = 0) off-resonance field of $B_{res} + B_m/2$, which nicely reproduced the initial time oscillation of PDT (Figure S1). The absence of hyperpolarization in the EPR signal can also be rationalized to the relatively long interval (~8 μs) between the laser pulse arrival and crossing of the resonance field in comparison to the T_{1e} of PDT (0.79 μs). Thus, when the laser was given an offset, Δt_{las}, with respect to the start of the field cycle scan, a strong emissive polarization could be clearly seen (Figure 5). Notably, a

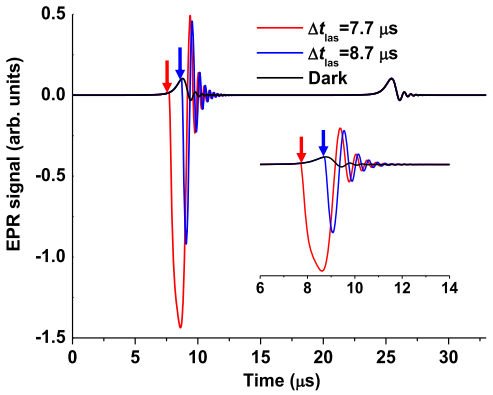

Figure 5. Simulation of the RSEPR time profile of the PDT molecule based on time-dependent Bloch equations under dark (blue) and after a laser pulse for two different laser offsets Δt_{las} = +7.7 μs (red) and Δt_{las} = +8.7 μs (blue) (the corresponding colored arrows mark the arrival of the laser pulse). Simulation parameters: P_S = 0, P_T/P_{eq} = −10; the other parameters are the same as given in Figure 4. The inset shows the zoomed region of the first half cycle. Note that the initial time (Torrey) oscillations of Figure 4 are reduced significantly as the laser is incident close to the exact resonance position. This further supports the assignment of the initial time oscillations of Figure 4 to Torrey oscillations.

comparison of the EPR profile for Δt_{las} = +7.7 and +8.7 μs revealed that the maximum hyperpolarization does not correlate with the arrival of the laser pulse at the peak of the resonance position (Δt_{las} = 8.7 μs). The optimum Δt_{las} should depend on the molecular parameters like k_{qt} and T_{1e}, which, in turn, can be obtained from TREPR experiments (and also on the experimental parameters like rapid scan frequency and the instrument response time). Thus, these results highlight the need for proper synchronization of the laser pulse with respect to the field scan cycle to obtain the maximum hyperpolarization in the RSEPR spectrum.

Having rationalized the hyperpolarization behavior of the PDT molecule in the RSEPR experiment, I next performed the simulations for the current molecule of interest, Anq1Pr (Chart S1), in its unlabeled form containing the usual ^{1}H and ^{14}N isotopes. For the simulations to represent the proposed hyperpolarized imaging experiment as close as possible, realistic values of all of the parameters were needed. To this end, the values of the parameters related to hyperpolarization generation, k_{qs}, k_{qt}, T_{1e}, T_{2e}, P_S, and P_T, for Anq1PR were obtained from its earlier optical and TREPR studies.[31] However, since a hyperpolarized RSEPR experiment has not been performed yet, the optimum values of f_m and B_m were not available. So, their optimum values were fixed as follows.

The field scanning rate, a, which is given by the product of f_m and B_m ($a \sim \pi \times f_m \times B_m$), is one of the critical factors in the RSEPR experiment that decides the choice of f_m and B_m. The guiding principle is that higher the f_m, higher is the sensitivity that can be achieved in an RSEPR experiment, as long as a or precisely $5a/(\sqrt{3}\pi\Delta H)$ is within the resonator bandwidth, $BW_{res} = \nu/2Q$ (where ν and Q are the frequency and the quality factor of the cavity resonator, respectively).[58] Moreover, to synchronize the field scan with the laser pulse, the maximum f_m

https://doi.org/10.1021/acs.jpcb.1c10920
J. Phys. Chem. B 2022, 126, 2715−2728

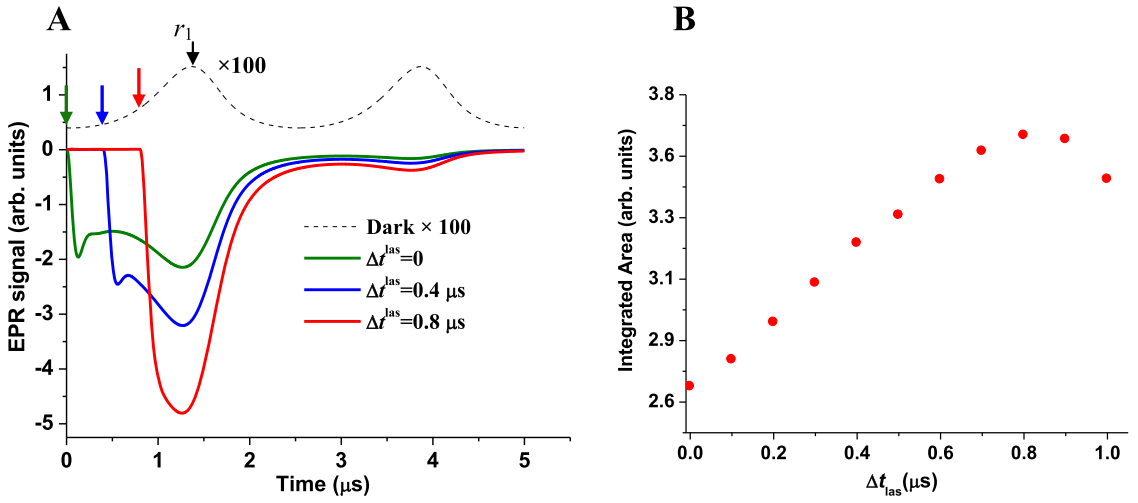

Figure 6. (A) Simulation of the RSEPR time profile of the Anq1Pr molecule based on Bloch equations under dark (black) and after a laser pulse for three different laser offsets $\Delta t_{las} = 0$ (green), $\Delta t_{las} = 0.4\ \mu s$ (blue), and $\Delta t_{las} = 0.8\ \mu s$ (red). The timing of the laser pulse for these curves is marked by the arrows (same colored). The black dotted trace is the 100 times amplified signal of the solid black trace. (B) Plot of the integrated signal of the RSEPR signal as a function of the laser offset. Simulation parameters: $f_m = 200$ kHz, $B_m = 3$ G, microwave power = 1 mW, $T_{1e} = 1\ \mu s$, $T_{2e} = 0.065\ \mu s$, $P_S = 0$, and $P_T/P_{eq} = -500$ (for other optical parameters, see the Materials and Methods). r_1 points to the resonance position where the intensities of thermal and ESP signals were compared.

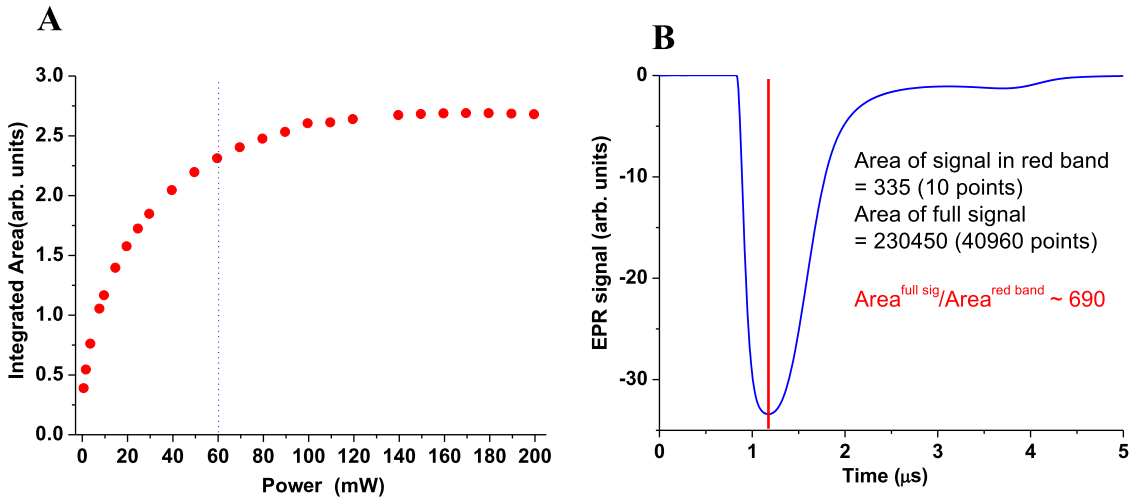

Figure 7. (A) Plot of the integrated area of the RSEPR signal of the Anq1Pr molecule as a function of the microwave power. The blue dotted line highlights the value for 60 mW. Other simulation parameters were the same as that of Figure 6. (B) RSEPR signal of the Anq1Pr molecule at a 60 mW microwave power. Note that the sum of 10 data points around the maximum signal (marked by the red band) was compared with the sum of the total signal of 40 960 data points. This was done to be compatible with the trace of Figure 3, which was recorded with 4096 data points.

that can be used would also be governed by the laser pulsing frequency f_{las}, which, in turn, is restricted by the spin−lattice relaxation time of the radical ($f_{las}^{-1} \geq 5T_{1e}$). Since T_{1e} of Anq1Pr is ∼1 μs, a maximum f_m (=f_{las}) value of 200 kHz can be used. Lastly, since the scan width should encompass at least one resonance line of nitroxides, which typically have a linewidth of 1 G, a B_m value of 3 G would be desired for nitroxides. These f_m and B_m values result in an a value of 1.9 MG·s^{-1}, which is close to the typical BW_{res} value of 1.6 MHz expected for an X-band resonator with $Q = 3000$. Thus, I used $f_m = 200$ kHz and $B_m = 3$ G for the RSEPR simulations of the Anq1Pr molecule.

Figure 6A shows the simulated RSEPR time profile for Anq1Pr in the absence and presence of laser irradiation with a hyperpolarization of 500 times the thermal spin polarization ($|P_T/P_{eq}| = 500$). In the absence of a laser, two broad lines were seen with no evidence of the wiggles, which is primarily due to the short T_{2e} of the Anq1Pr molecule. In the presence of laser irradiation, a strong emissive hyperpolarized signal was seen in the first half cycle. Notably, due to the reduced time interval between the two half cycles at f_m = 200 kHz, a small hyperpolarization is manifested even in the second half cycle. It is worth mentioning here that this behavior could prove beneficial in imaging experiments since just by comparing the intensities of the two half cycles, an estimate of T_{1e} can be obtained. This would be of particular relevance to the field of EPR oximetry, where oxygen profiles in the system of interest are related to the T_{1e} values of the spin probe.

Next, the effect of the laser offset, Δt_{las}, on the RSEPR signal of the Anq1Pr molecule was examined. To this end, the simulations were run with different values of Δt_{las} (Figure 6A) and the resulting integrated EPR signal intensity was plotted as a function of Δt_{las}. The plot (Figure 6B) revealed that the

https://doi.org/10.1021/acs.jpcb.1c10920
J. Phys. Chem. B 2022, 126, 2715−2728

maximum enhancement was seen for a Δt_{las} value of +0.8 μs, which corresponds to the arrival of laser approximately at the rising edge of the resonance signal (Figure 6A). Under these conditions, an enhancement of ~375 times was seen at the peak of the resonance position (r_1 in Figure 6A), which is almost similar to the enhancement that was obtained in the TREPR experiment of Anq1Pr (for trace in Figure 3, $S_{min}^{Pol}/S_{min}^{Bolt} \sim 300$). Thus, it may appear that the RSEPR does not result in any significant advantage for the sensitivity improvement compared to that of a TREPR detection scheme. However, the characteristic features by which RSEPR scores over CWEPR and even TREPR is its use of a large microwave (μw) power and a large number of repetitions. Thus, I next examined how these factors can improve the sensitivity that was obtained in the TREPR experiment of Figure 3.

First the effect of the microwave power was examined. Specifically, the hyperpolarized RSEPR time profile was simulated based on the Bloch equations for different microwave powers and the integrated intensity of the RSEPR time profile over one cycle was compared. Figure 7A shows such a plot. The results show that the power can safely be increased up to 60 mW without causing any significant saturation. This should result in an improvement of at least 6 times in the signal intensity compared to that of Figure 3 (which was acquired with 1 mW). It is worth pointing here that the use of such a high microwave power for the Anq1Pr molecule can be justified based on earlier RSEPR experiments on nitroxides where a power of 50−53 mW has successfully been used to improve the SNR.[46,47] Notably, the authors[47] also found that the source power does not contribute to the noise up to 50 mW of the microwave power, thereby indicating that the abovementioned value of 60 mW should not result in any significant increase of noise.

Next, the advantage of larger averaging in RSEPR was taken into account. Specifically, compared to three averages that were acquired in 0.2 s of Figure 3, the number of averages that are possible in the RSEPR experiment for the same acquisition time is 40 000 (≡200 kHz × 0.2 s). This would result in the improvement in SNR by $\sqrt{40\,000/3}$, compared to Figure 3. It should be noted that the repetition rate in the TREPR experiment of Anq1Pr (Figure 3) could not be increased to 200 kHz primarily because the maximum repetition rate of our Nd:YAG laser was 30 Hz. On the other hand, since the OH-EPRI experiment is based on a two-photon excitation, which needs a femtosecond (fs) laser, there is no problem in achieving signal averaging at a rate of 200 kHz, as commercial fs lasers with repetition rates as high as 80 MHz are available.

Further enhancement in the SNR can be achieved if the entire (integrated) area of the signal over one full cycle is used as a measure of the signal intensity, compared to a single point value that was used in Figure 3. After performing such an integration for the RSPER time profile of the Anq1Pr molecule (Figure 7B), an improvement in the signal by a factor of ~690 can be achieved. In a real situation, the presence of noise in the signal would possibly result in the reduction of the maximum enhancement of 690. However, with digital filtering schemes or with a simulation of the experimental curve followed by the integration of the simulated curve, the maximum enhancement factor of 690 can still be realized.

Thus, combining the enhancements due to higher averaging, higher microwave power, and full signal integration, the RSEPR can improve the SNR by a factor of $\sqrt{\frac{40\,000}{3}} \times 6 \times 690 = 4.8 \times 10^5$ times, compared to that of the TREPR signal of Figure 3. Thus, the sensitivity that can be achieved in an RSEPR experiment of hyperpolarized Anq1Pr at RT under nonlossy sample conditions is $\sim 9 \times 10^6$ spins·G^{-1}·Hz$^{-1/2}$, which corresponds to almost 5 orders of magnitude improvement compared to the TREPR detection of Anq1Pr.

Finally, the effects of a lossy sample condition (expected for a cellular system) and a microresonator (required for two-photon excitation) were examined. In this regard, the results of earlier sensitivity studies in microresonators[9,34,35,59−62] (summarized in Table S1) reveal that microresonators improve the thermal sensitivity of volume-limited samples (<μL) compared to the cavity resonators primarily via maximizing the filling factor of the sample. A notable aspect in this regard is that even for an aqueous sample at RT, a thermal sensitivity of 5.3×10^7 spins·Hz$^{-1/2}$ has been demonstrated in a surface loop-gap microresonator.[60] However, this experiment was performed on a deuterated trityl radical (which has a very narrow linewidth compared to unlabeled nitroxyls), employing an FTEPR method, and the microwave frequency was 16 GHz. I extrapolated this value (Appendix SII) to the conditions of an aqueous nitroxide solution at the X-band frequency and the CWEPR mode of operation and obtained a value of 2×10^{10} spins·G^{-1}·Hz$^{-1/2}$ for the thermal sensitivity at RT in the same microresonator. Comparing this value with the typical CWEPR thermal sensitivity of $10^{11}-10^{12}$ spins·G^{-1}·Hz$^{-1/2}$ for a cavity-based resonators,[43] it should be safe to assume that an improvement of about 1 order of magnitude can be achieved via the use of microresonators. Thus, the detection sensitivity for a hyperpolarized RSEPR signal would improve to ~10^6 spins·G^{-1}·Hz$^{-1/2}$ via the use of a microresonator, which is precisely the desired value to achieve a subcellular resolution. Thus, the abovementioned results indicate that a 3D spatial resolution of ~2 fL for a 1 mM spin probe solution should be achievable via RSEPR detection of a hyperpolarized Anq1pr molecule.

In the abovementioned analysis leading to a high spatial resolution, it was assumed that all of the molecules in the 2 fL volume were photoexcited (for the concentration of 1 mM, the number of molecules in 2 fL is ~10^6). It is only then that these molecules would generate a hyperpolarization and hence contribute to the EPR signal. Since the photoexcitation is via a two-photon (2P) mechanism, I next considered whether it would be possible to achieve this condition, i.e., of the 2P excitation of all of the pixel element molecules for a 1 mM solution of an anthraquinone-based CR molecule (like Anq1Pr).

Two-Photon Excitation (2PE) of Anthraquinone-Based CR Spin Probes. Analogous to the molar extinction coefficient, ε, which quantifies the one-photon excitation efficiency, the 2PE efficiency of a molecule is quantified by its 2PE cross section, δ, which is represented in units of Göppert-Mayer (GM) (1 GM = 10^{-50} cm^4·s·molecule^{-1}·photon^{-1}).[33] Efficient 2PE probes have δ values in the range of 10^2-10^5 GM,[63−67] whereas the widely used fluorophores such as fluorescein, coumarin, etc. have δ values in the range of 30−50 GM.[68] To the best of my knowledge, the δ value of anthraquinone is not reported in the literature, possibly because of its nonfluorescent nature. So I referred to the δ values of structurally similar small-molecule fluorophores such as anthracene and flavin mononucleotide (FMN), whose δ values have been measured to be 3 GM (λ^{ex} = 532 nm)[69] and 1 GM (λ^{ex} = 900 nm),[70] respectively, and assumed a δ value of 1 GM for the anthraquinone moiety for further calculations.

https://doi.org/10.1021/acs.jpcb.1c10920
J. Phys. Chem. B 2022, 126, 2715−2728

The number of molecules, N_m, excited by a TEM_{00} laser pulse in a confocal volume defined by length z and beam waist w (Figure S2) is given by[71]

$$N_m = \frac{E_P^2 \delta \rho^2 z}{\sqrt{2}\pi (hc)^2 \tau w^2} \quad (7)$$

where E_P is the pulse energy, τ is the laser pulse width, λ is the laser wavelength, c is the velocity of light, h is Planck's constant, and ρ is the concentration in molecules cm^{-3}. Safe operating conditions for the cell restrict the maximum value of E_P that can be used in a 2P experiment.[33] In this regard, a guiding principle is that the average laser power (P_W) should be ≤5 mW for safe operation on cells.[72,73] Since P_W is a product of the E_P and the laser repetition frequency f_{las}, the safe value of E_P depends on f_{las}.[74−77] Thus, for the present case of f_{las} = 200 kHz, the maximum E_P that can be used is 25 nJ per pulse. In optical imaging experiments,[74−78] E_P values of up to 60 nJ have been used for f_{las} = 250 kHz, without causing any significant phototoxicity.[76] Hence, the present value of 25 nJ for f_{las} = 200 kHz should prove to be safe in OH-EPRI experiments.

Next, I determined the number of photoexcited Anq1Pr molecules (N_m) created via 2PE in a confocal volume of 2 μm^3 (i.e., 2 fL) and compared it with the number of molecules present in this volume, N_c (1.2×10^6 for a 1 mM concentration of the spin probe). Using eq 7 along with the following fs laser parameters that would be applicable for the proposed hyperpolarized imaging experiment of 1 mM Anq1Pr: λ = 700 nm, τ = 100 fs, N = 200 kHz, E_P = 25 nJ, w = 0.7 μm, and z = 1 μm (which gives a confocal volume of ∼2 fL assuming it to be an ellipsoid), the number of photoexcited molecules was estimated to be $N_m \sim 2 \times 10^6$, which is larger than N_c. Obviously, N_m can never be greater than N_c, and this result could possibly be due to limitations of eq 7 at high laser energies. But what is important in the current context is that N_m is not less than N_c, which indicates that the fs laser pulse of 25 nJ is capable of exciting all of the molecules present in the irradiated volume via a 2P process. Thus, the 2P excitation efficiency of the Anq1Pr molecule indeed supports the feasibility of achieving a 2 fL resolution in an OH-EPRI experiment.

Collating all of the abovementioned results, it can be summarized that the anthraquinone-based CR nitroxyl molecules should potentially result in achieving a spatial resolution of ∼2 μm^3 in the EPRI experiments at X-band frequencies, which would enable performing subcellular imaging experiments. Notably, this resolution should be achievable even for isotopically unlabeled nitroxyls.

DISCUSSION

The present work examines the feasibility of harnessing the electron spin hyperpolarization in conventional EPR imaging experiments to improve its spatial resolution. To this end, the rapid scan method of EPR acquisition was considered due to its known potential to achieve both an enhanced sensitivity and fast time resolution.[49] The time-dependent Bloch equation simulations of a hyperpolarized Anq1pr molecule revealed that a sensitivity of 2×10^6 spins·G^{-1}·$Hz^{-1/2}$ at RT could be achieved via RSEPR detection if (i) Anq1Pr can be hyperpolarized with an ESP magnitude of 500 times the thermal ESP, (ii) a microresonator with a thermal CWEPR sensitivity of at least 10^{10} spins·G^{-1}·$Hz^{-1/2}$ for aqueous nitroxyl (containing all magnetic nuclei in their natural abundance) samples at RT is available, and (iii) a fs laser with f_{las} = 200 kHz and E_P = 25 nJ is available. Notably, based on the existing technological/scientific developments, the majority of the abovementioned requirements can be satisfied. For example, fs lasers with f_{las} = 200 kHz and E_P = 25 nJ in the 700−800 nm wavelength region are easily accessible. The field of microresonators is also continuously progressing, with the thermal FTEPR sensitivities of 10^7−10^8 spins·G^{-1}·$Hz^{-1/2}$ for aqueous samples already demonstrated.[79] Other requirements of the OH-EPRI experiment such as scanning mirrors and high-speed data acquisition modules[80] may also be adapted from existing 2P confocal imaging setups.

The necessary instrumentation, therefore, is within the present-day technological capability. On the other hand, what is of prime importance is the design and synthesis of photostable anthraquinone-based CR molecules. This is especially important in view of the severe photoinstability of the ANCOOT and Anq1Pr molecules in protic solvents[31,36] and the known chemical instability of the radicals in reducing cellular environments.[81] Thus, a more robust design of the spin probes would govern the success of the proposed method. In addition, the large hyperpolarization in the Anq1Pr molecule has been demonstrated so far only in nonpolar solvents (primarily due to solubility constraints). Thus, designing water-soluble spin probes and understanding their spin dynamics in water would also be an essential aspect governing the future of OH-EPRI.

As discussed above, the success of OH-EPRI also rests critically on the 2P excitation efficiency of anthraquinone. In the present work, a δ value of 1 GM (at 700 nm) was assumed for anthraquinone, which almost falls toward the lower side of the δ values of typical chromophores. However, if the δ value is even lower than 1 GM, the spatial resolution would deteriorate correspondingly. In this regard, a potential strategy would be to employ a 2P sensitizer molecule with a large δ value. Such a strategy is widely used in a variety of fields where the chromophore of interest has a small δ value.[82,83] A sensitizer with a large δ value will also allow the experiments to be carried at lower concentrations of the spin probe concentration and/or a lower pulse energy E_P, which would be very beneficial to reduce the spin probe-induced or photoinduced toxicity to the cells. In addition, the use of a sensitizer would allow a preferential 2P excitation of the chromophore over the radical by selectively tethering of the sensitizer to the chromophore.

In the field of EPR imaging involving live animals, low frequencies (ν^{EPR} ∼ 250 MHz to 1 GHz) are generally preferred.[1,84] This is primarily aimed at reducing the dielectric absorption of water. Although the precise frequency dependence of the sensitivity of EPR spectrometers depends on many parameters such as a resonator, Boltzmann factor, polarity of the sample nature, etc.,[85] the Boltzmann factor always changes unfavorably with the lowering of ν^{EPR}. Thus, it is quite natural to examine if a large electron hyperpolarization would help to overcome the sensitivity loss due to the lower Boltzmann factor in the low-frequency EPR imaging. However, the specific gains due to the hyperpolarization will depend on the frequency dependence of hyperpolarization mechanisms and the light penetrability for live animal imaging. The former problem has not been addressed yet. However, given the possibility of fine-tuning the structural parameters of spin probe molecules to adapt for different ν^{EPR}, as has been done earlier to synthesize potential molecules for high-field dynamic nuclear polarization (DNP) applications,[56] it should be possible to design efficient EHP-generating spin probe molecules even at lower ν^{EPR}.

The second issue with the light penetration, which originates due to strong absorbance/scattering of the light by tissues, is also

https://doi.org/10.1021/acs.jpcb.1c10920
J. Phys. Chem. B 2022, 126, 2715−2728

faced in the conventional optical techniques, such as fluorescence-based imaging, photodynamic therapy, etc. However, as demonstrated in these optical techniques, the use of IR light alleviates this issue to a large extent.[63,66] Typically, either the chromophore itself absorbs the IR light and undergoes a two/multiphoton (MPI) excitation or a sensitizer is used, which has a large MPI cross section for IR excitation. Similar strategies could be adapted even for the present case too. Thus, the present proposed method could benefit even the field of live animal EPR imaging.

There are other techniques such as magnetic resonance force microscopy (MRFM),[86] scanning tunneling microscopy,[87] and optically detected magnetic resonance (ODMR) with nitrogen-vacancy (NV) paramagnetic centers,[88,89] which have very high sensitivity and have demonstrated the detection of even a single electron spin. However, to achieve such high sensitivity, these techniques need very special conditions, such as very low temperature, very high vacuum (MRFM, STM), or the sample has to be within a 10 nm radius of the detector (NV center). A very recent demonstration of the NV center for RT imaging is quite encouraging in this regard. However, it needs the linking of the paramagnetic molecule to the NV tip to ensure that it remains within the 10 nm zone of the NV center.[90] Thus, these techniques are more suitable for either surface-based 2D imaging or for an isolated molecule such as proteins or DNA, or a combination of both. Adapting them to a cellular scale for 3D imaging under ambient conditions is very difficult. In contrast, the present proposal of the OH-EPRI method is not restricted by these conditions. In addition, it should be noted that the abovementioned methods are based on a sensitive detection method, while the OH-EPRI method is based on creating a strong magnetization in the sample. Thus, in principle, all of the abovementioned techniques could be adapted for optical hyperpolarized signal detection, which could either enable a RT operation of the samples or impart a 3D imaging capability to them.

Finally, the OH-EPRI method would not only enable a subcellular resolution for EPRI of biological samples at RT but could also offer some additional advantages. For example, the technique is not restricted to nitroxides but other radicals such as BDPA or trityl could also be used in place of nitroxides, as long as they can be tethered to a suitable chromophore. CR spin probes involving such radicals have already been synthesized and examined for hyperpolarization generation.[28] Next, different radicals can be selectively observed by employing wavelength-specific chromophores/sensitizers. Thus, nitroxides could be selectively targeted to different parts of the cell, such as cell membrane, mitochondria, or nucleus, and imaged accordingly. Furthermore, the OH-EPRI method can also be combined with the powerful imaging method of proton−electron double resonance imaging (PEDRI),[91] which is primarily a dynamic nuclear polarization (DNP) method used for electron spin imaging. In this regard, the use of a laser excitation, instead of a microwave, in the hyperpolarized PEDRI experiment would not only generate a large hyperpolarized PEDRI signal but would also enable a complete microwave-free mode of operation, which could prove highly beneficial for biological samples. Lastly, via DNP, the OH-EPRI method could also possibly benefit the widely used nuclear magnetic resonance imaging (MRI) too.

CONCLUSIONS

Achieving a subcellular spatial resolution in the imaging of biological samples doped with nitroxide molecules at room temperature (RT) and without any isotopic labeling is highly desired. The present work proposes a novel in vitro EPR imaging method, termed OH-EPRI, which is primarily based on the generation of a large hyperpolarization in nitroxide radicals via a two-photon excitation, followed by its detection via the rapid scan EPR method. Simulations based on time-dependent Bloch equations revealed that a sensitivity of up to 10^6 spins·G^{-1}·$Hz^{-1/2}$ at RT could be achieved if the nitroxides can be hyperpolarized with an ESP magnitude of 500 times the thermal ESP and an X-band microresonator with a CWEPR sensitivity of at least 10^{10} spins·G^{-1}·$Hz^{-1/2}$ for an aqueous nitroxyl sample at RT is available. The majority of these requirements can be realized in the near future, paving the way for its easy implementation.

One of the unique aspects of the OH-EPRI method is that it does not need any magnetic field gradient to achieve a spatial resolution and is thus immune to problems associated with field gradients as well as the large linewidths of isotopically unlabeled nitroxyls (i.e., all of the nuclei in their natural abundance). This would benefit cancer research, where the unlabeled nitroxides either in the form of antioxidants or labeled with chemotherapeutic drugs are widely used.[92−96] Even the detection of reactive oxygen species (ROS) such as $OH^{\bullet}$, $O_2^{\bullet-}$, etc., which play an important role in cancer metastasis are detected via unlabeled nitroxide-based spin traps.[97−100] In this regard, OH-EPRI would be very beneficial to give subcellular details of ROS production, an aspect currently not possible with conventional EPRI. Furthermore, for properties like microviscosity, pH, and redox status, polarity for which the nitroxides are highly sensitive to,[19,32,101−106] the OH-EPRI method can allow obtaining such information in a highly cell-localized manner.

Lastly, given that fields like quantum computing[107,108] require selective addressing and faithful readout of spins, the current proposal of using a two-photon excitation for generating a hyperpolarized EPR signal can potentially address both of these concerns. Thus, it would not be wrong to conceive that the OH-EPRI, which assimilates the benefits of both EPR and the optical microscopy, would benefit diverse fields in the near future.

ASSOCIATED CONTENT

Supporting Information

The Supporting Information is available free of charge at https://pubs.acs.org/doi/10.1021/acs.jpcb.1c10920.

Structures and acronyms of the molecule used in this work (Chart S1); additional figures; sensitivity of the microresonator-based EPR spectrometers for thermal electron spin polarization at room temperature (~300 K) (Appendix SI), estimation of the sensitivity of a microresonator-based CWEPR spectrometer at room temperature (RT) for aqueous samples (Appendix SII); hyperpolarization in chromophore−radical (C−R) systems (Appendix SIII); data acquisition and processing (Appendix SIV) (PDF)

AUTHOR INFORMATION

Corresponding Author

Vinayak Rane − *Radiochemistry Division, Bhabha Atomic Research Centre, Mumbai 400085, India;* Present Address: Indian Institute of Geomagnetism, Plot 5, Sector

https://doi.org/10.1021/acs.jpcb.1c10920
J. Phys. Chem. B 2022, 126, 2715−2728

18, New Panvel (W), Navi Mumbai 410218, India; orcid.org/0000-0001-6043-3586; Phone: +91-22-25690513; Email: rane.vinayak@gmail.com

Complete contact information is available at: https://pubs.acs.org/10.1021/acs.jpcb.1c10920

Notes

The author declares no competing financial interest.

■ ACKNOWLEDGMENTS

This work was performed in the time-resolved EPR facility at the Tata Institute of Fundamental Research (TIFR), Mumbai (India). The author acknowledges Prof. Jyotishman Dasgupta, TIFR, for providing access to this facility. He sincerely thanks Prof. Ranjan Das, TIFR Mumbai, and Prof. Pranav Shirhatti, TIFR Hyderabad, for their constructive criticism as well as for proofreading the manuscript. He also thanks Dr. Krishnendu Kundu, National Magnetic Resonance Laboratory, Florida, for giving valuable inputs. He would also like to acknowledge Dr. William K. Myers, Centre for Advanced ESR, for fruitful discussion regarding rapid scan EPR.

■ REFERENCES

(1) Eaton, G. R.; Eaton, S. S.; Ohno, K. *EPR Imaging and In Vivo EPR*; CRC Press: Boca Raton, FL, 2018.
(2) Swartz, H. M.; Berliner, L. J. *In Vivo* EPR. *Biological Magnetic Resonance*; Kluwer Academi: New York, 2003; Vol. *18*.
(3) Epel, B.; Kotecha, M.; Halpern, H. J. In Vivo Preclinical Cancer and Tissue Engineering Applications of Absolute Oxygen Imaging Using Pulse EPR. *J. Magn. Reson.* **2017**, *280*, 149−157.
(4) Suhovoy, E.; Mishra, V.; Shklyar, M.; Shtirberg, L.; Blank, A. Direct Micro-Imaging of Point Defects in Bulk SiO 2, Applied to Vacancy Diffusion and Clustering. *EPL* **2010**, *90*, No. 26009.
(5) Sathiya, M.; Leriche, J. B.; Salager, E.; Gourier, D.; Tarascon, J. M.; Vezin, H. Electron Paramagnetic Resonance Imaging for Real-Time Monitoring of Li-Ion Batteries. *Nat. Commun.* **2015**, *6*, No. 6276.
(6) Blank, A. Scheme for a Spin-Based Quantum Computer Employing Induction Detection and Imaging. *Quantum Inf. Process.* **2013**, *12*, 2993−3006.
(7) Ahmad, R.; Kuppusamy, P. Theory, Instrumentation, and Applications of Electron Paramagnetic Resonance Oximetry. *Chem. Rev.* **2010**, *110*, 3212−3236.
(8) Davies, M. J. Detection and Characterisation of Radicals Using Electron Paramagnetic Resonance (EPR) Spin Trapping and Related Methods. *Methods* **2016**, *109*, 21−30.
(9) Shtirberg, L.; Twig, Y.; Dikarov, E.; Halevy, R.; Levit, M.; Blank, A. High-Sensitivity Q-Band Electron Spin Resonance Imaging System with Submicron Resolution. *Rev. Sci. Instrum.* **2011**, *82*, No. 043708.
(10) Xu, C.; Xu, W.; Yang, Z.; Li, S.; Wang, Y.; Hua, J. A Turn-on Mitochondria-Targeted near-Infrared Fluorescent Probe with a Large Stokes Shift for Detecting and Imaging Endogenous Superoxide Anion in Cells. *J. Photochem. Photobiol., A* **2021**, *415*, No. 113304.
(11) Ji, K.; Shan, J.; Wang, X.; Tan, X.; Hou, J.; Liu, Y.; Song, Y. Rational Design of Near-Infrared Fluorescent Probes for Superoxide Anion Radical: Enhancement of Self-Stability and Sensitivity by Self-Immolative Linker. *Free Radical Biol. Med.* **2021**, *167*, 36−44.
(12) Lu, D.; Zhou, L.; Wang, R.; Zhang, X. B.; He, L.; Zhang, J.; Hu, X.; Tan, W. A Two-Photon Fluorescent Probe for Endogenous Superoxide Anion Radical Detection and Imaging in Living Cells and Tissues. *Sens. Actuators, B* **2017**, *250*, 259−266.
(13) Kalyanaraman, B.; Darley-Usmar, V.; Davies, K. J. A.; Dennery, P. A.; Forman, H. J.; Grisham, M. B.; Mann, G. E.; Moore, K.; Roberts, L. J.; Ischiropoulos, H. Measuring Reactive Oxygen and Nitrogen Species with Fluorescent Probes: Challenges and Limitations. *Free Radical Biol. Med.* **2012**, *52*, 1−6.
(14) Wardman, P. Fluorescent and Luminescent Probes for Measurement of Oxidative and Nitrosative Species in Cells and Tissues: Progress, Pitfalls, and Prospects. *Free Radical Biol. Med.* **2007**, *43*, 995−1022.
(15) Blank, A.; Dikarov, E.; Shklyar, R.; Twig, Y. Induction-Detection Electron Spin Resonance with Sensitivity of 1000 Spins: En Route to Scalable Quantum Computations. *Phys. Lett. A* **2013**, *377*, 1937−1942.
(16) Yamada, K. I.; Murugesan, R.; Devasahayam, N.; Cook, J. A.; Mitchell, J. B.; Subramanian, S.; Krishna, M. C. Evaluation and Comparison of Pulsed and Continuous Wave Radiofrequency Electron Paramagnetic Resonance Techniques for in Vivo Detection and Imaging of Free Radicals. *J. Magn. Reson.* **2002**, *154*, 287−297.
(17) Subramanian, S.; Krishna, M. C. Dancing with the Electrons: Time-Domain and CW In Vivo EPR Imaging. *Magn. Reson. Insights* **2008**, *2*, 43−74.
(18) Levêque, P.; Leprince, J. G.; Bebelman, S.; Devaux, J.; Leloup, G.; Gallez, B. Spectral Spatial Electron Paramagnetic Resonance Imaging as a Tool to Study Photoactive Dimethacrylate-Based Dental Resins. *J. Magn. Reson.* **2012**, *220*, 45−53.
(19) Epel, B.; Sundramoorthy, S. V.; Krzykawska-Serda, M. M.; Maggio, M. C.; Tseytlin, M.; Eaton, G. R.; Eaton, S. S.; Rosen, G. M.; Kao, J. P.; Halpern, H. J. Imaging Thiol Redox Status in Murine Tumors in Vivo with Rapid-Scan Electron Paramagnetic Resonance. *J. Magn. Reson.* **2017**, *276*, 31−36.
(20) Hyodo, F.; Matsumoto, S.; Devasahayam, N.; Dharmaraj, C.; Subramanian, S.; Mitchell, J. B.; Krishna, M. C. Pulsed EPR Imaging of Nitroxides in Mice. *J. Magn. Reson.* **2009**, *197*, 181−185.
(21) Blättler, C.; Jent, F.; Paul, H. A Novel Radical-Triplet Pair Mechanism for Chemically Induced Electron Polarization (CIDEP) of Free Radicals in Solution. *Chem. Phys. Lett.* **1990**, *166*, 375−380.
(22) Goudsmit, G. H.; Paul, H.; Shushin, A. I. Electron Spin Polarization in Radical-Triplet Pairs. Size and Dependence on Diffusion. *J. Phys. Chem. A* **1993**, *97*, 13243−13249.
(23) Fujisawa, J. I.; Ishii, K.; Ohba, Y.; Iwaizumi, M.; Yamauchi, S. Electron Spin Polarization Transfer from Excited Triplet Porphyrins to a Nitroxide Radical via a Spin Exchange Mechanism. *J. Phys. Chem. B* **1995**, *99*, 17082−17084.
(24) Kobori, Y.; Takeda, K.; Tsuji, K.; Kawai, A.; Obi, K. Exchange Interaction in Radical-Triplet Pairs: Evidences for CIDEP Generation by Level Crossings in Triplet-Doublet Interactions. *J. Phys. Chem. A* **1998**, *102*, 5160−5170.
(25) Kandrashkin, Y.; van der Est, A. Light-Induced Electron Spin Polarization in Rigidly Linked, Strongly Coupled Triplet − Doublet Spin Pairs. *Chem. Phys. Lett.* **2003**, *379*, 574−580.
(26) Tarasov, V. F.; Islam, S. S. M.; Ohba, Y.; Forbes, M. D. E.; Yamauchi, S. Multifrequency TREPR Investigation of Excited-State ZnTPP/Nitroxide Radical Complexes. *Appl. Magn. Reson.* **2011**, *41*, 175−193.
(27) Dyar, S. M.; Margulies, E. A.; Horwitz, N. E.; Brown, K. E.; Krzyaniak, M. D.; Wasielewski, M. R. Photogenerated Quartet State Formation in a Compact Ring-Fused Perylene-Nitroxide. *J. Phys. Chem. B* **2015**, *119*, 13560−13569.
(28) Avalos, C. E.; Richert, S.; Socie, E.; Karthikeyan, G.; Casano, G.; Stevanato, G.; Kubicki, D. J.; Moser, J. E.; Timmel, C. R.; Lelli, M.; Rossini, A. J.; Ouari, O.; Emsley, L. Enhanced Intersystem Crossing and Transient Electron Spin Polarization in a Photoexcited Pentacene-Trityl Radical. *J. Phys. Chem. A* **2020**, *124*, 6068−6075.
(29) Kandrashkin, Y. E.; Van Der Est, A. The Triplet Mechanism of Electron Spin Polarization in Moderately Coupled Triplet-Doublet Rigid Complexes as a Source of the Enhanced +1/2 ↔ −1/2 Transitions. *J. Chem. Phys.* **2019**, *151*, No. 184301.
(30) Takahashi, H.; Iwama, M.; Akai, N.; Shibuya, K.; Kawai, A. Pulsed EPR Study on Large Dynamic Electron Polarisation Created in the Quenching of Photo-Excited Xanthene Dyes by Nitroxide Radicals in Aqueous Solutions. *Mol. Phys.* **2014**, *112*, 1012−1020.
(31) Rane, V. Achieving Maximal Enhancement of Electron Spin Polarization in Stable Nitroxyl Radicals at Room Temperature. *J. Phys. Chem. B* **2021**, *125*, 5620−5629.

(32) Khramtsov, V. V. Vivo Spectroscopy and Imaging of Nitroxide Probes. In *Nitroxides—Theory, Experiment and Applications*; Kokorin, A. I. E., Ed.; InTech: Rijeka, Croatia, 2012; pp 317−346.
(33) Pawley, J. B. *Handbook of Biological Confocal Microscopy*, 3rd ed.; Pawley, J. B., Ed.; Springer: New York, 2006.
(34) Boero, G.; Bouterfas, M.; Massin, C.; Vincent, F.; Besse, P. A.; Popovic, R. S.; Schweiger, A. Electron-Spin Resonance Probe Based on a 100 Mm Planar Microcoll. *Rev. Sci. Instrum.* **2003**, *74*, 4794−4798.
(35) Abhyankar, N.; Agrawal, A.; Shrestha, P.; Maier, R.; McMichael, R. D.; Campbell, J.; Szalai, V. Scalable Microresonators for Room-Temperature Detection of Electron Spin Resonance from Dilute, Sub-Nanoliter Volume Solids. *Sci. Adv.* **2020**, *6*, No. eabb0620.
(36) Tripathi, A.; Rane, V. Toward Achieving the Theoretical Limit of Electron Spin Polarization in Covalently Linked Radical-Chromophore Dyads. *J. Phys. Chem. B* **2019**, *123*, 6830−6841.
(37) Rane, V.; Das, R. Distance Dependence of Electron Spin Polarization during Photophysical Quenching of Excited Naphthalene by TEMPO Radical. *J. Phys. Chem. A* **2015**, *119*, 5515−5523.
(38) Stoner, J. W.; Szymanski, D.; Eaton, S. S.; Quine, R. W.; Rinard, G. A.; Eaton, G. R. Direct-Detected Rapid-Scan EPR at 250 MHz. *J. Magn. Reson.* **2004**, *170*, 127−135.
(39) Rozenshtein, V.; Berg, A.; Stavitski, E.; Levanon, H.; Franco, L.; Corvaja, C. Electron Spin Polarization of Functionalized Fullerenes. Reversed Quartet Mechanism. *J. Phys. Chem. A* **2005**, *109*, 11144−11154.
(40) Tripathi, A. K.; Rane, V.; Kundu, S.; Das, R. A Phenomenological Scheme for Reversed Quartet Mechanism of Electron Spin Polarization in Covalently Linked Systems of Chromophore and Free Radical: Determination of Magnitude of Polarization and Application to PyreneO Linked Molecules. *J. Chem. Phys.* **2019**, *151*, No. 154305.
(41) Zhao, L.; Kroenke, C. D.; Song, J.; Piwnica-Worms, D.; Ackerman, J. J. H.; Neil, J. J. Intracellular Water-Specific MR of Microbead-Adherent Cells: The HeLa Cell Intracellular Water Exchange Lifetime. *NMR Biomed.* **2008**, *21*, 159−164.
(42) Schmalbein, D.; Maresch, G. G.; Kamlowski, A.; Höfer, P. The Bruker High-Frequency-EPR System. *Appl. Magn. Reson.* **1999**, *16*, 185−205.
(43) Weil, J. A.; Bolton, J. R.; Wertz, J. E.; Buckmaster, H. A. *Electron Paramagnetic Resonance: Elementary Theory and Practical Applications*, 2nd ed.; John Wiley & Sons, Inc.: New Jersey, 1995; Vol. *48*.
(44) Belford, R. L.; Clarkson, R. B. Multifrequency Electron Paramagnetic Resonance Spectroscopy. *Advances in Chemistry*; American Chemical Society, 1992.
(45) Eaton, S. S.; Shi, Y.; Woodcock, L.; Buchanan, L. A.; McPeak, J.; Quine, R. W.; Rinard, G. A.; Epel, B.; Halpern, H. J.; Eaton, G. R. Rapid-Scan EPR Imaging. *J. Magn. Reson.* **2017**, *280*, 140−148.
(46) Mitchell, D. G.; Rosen, G. M.; Tseitlin, M.; Symmes, B.; Eaton, S. S.; Eaton, G. R. Use of Rapid-Scan EPR to Improve Detection Sensitivity for Spin-Trapped Radicals. *Biophys. J.* **2013**, *105*, 338−342.
(47) Mitchell, D. G.; Quine, R. W.; Tseitlin, M.; Eaton, S. S.; Eaton, G. R. X-Band Rapid-Scan EPR of Nitroxyl Radicals. *J. Magn. Reson.* **2012**, *214*, 221−226.
(48) Mitchell, D. G.; Tseitlin, M.; Quine, R. W.; Meyer, V.; Newton, M. E.; Schnegg, A.; George, B.; Eaton, S. S.; Eaton, G. R. X-Band Rapid-Scan EPR of Samples with Long Electron Spin Relaxation Times: A Comparison of Continuous Wave, Pulse and Rapid-Scan EPR. *Mol. Phys.* **2013**, *111*, 2664−2673.
(49) Eaton, S. S.; Quine, R. W.; Tseitlin, M.; Mitchell, D. G.; Rinard, G. A.; Eaton, G. R. Rapid-Scan Electron Paramagnetic Resonance. *Multifrequency Electron Paramagnetic Resonance: Data and Techniques*; John Wiley & Sons, Inc., 2014; pp 3−67.
(50) Verma, N. C.; Fessenden, R. W. Time Resolved ESR Spectroscopy. IV. Detailed Measurement and Analysis of the ESR Time Profile. *J. Chem. Phys.* **1976**, *65*, 2139−2155.
(51) Verma, N. C.; Fessenden, R. W. Time Resolved ESR Spectroscopy. II. The Behavior of H Atom Signals. *J. Chem. Phys.* **1973**, *58*, 2501−2506.
(52) Atkins, P. W.; Dobbs, A. J.; McLauchlan, K. A. Transient Nutations in Electron Spin Resonance. *Chem. Phys. Lett.* **1974**, *25*, 105−107.
(53) Kawai, A.; Shibuya, K. Charge-Transfer Controlled Exchange Interaction in Radical-Triplet Encounter Pairs as Studied by FT-EPR Spectroscopy. *J. Phys. Chem. A* **2007**, *111*, 4890−4901.
(54) Kawai, A.; Shibuya, K. Electron Spin Dynamics in a Pair Interaction between Radical and Electronically-Excited Molecule as Studied by a Time-Resolved ESR Method. *J. Photochem. Photobiol., C* **2006**, *7*, 89−103.
(55) Blank, A.; Levanon, H. Triplet Radical Interaction. Direct Measurement of Triplet Polarization Transfer by Fourier Transform Electron Paramagnetic Resonance. *J. Phys. Chem. A* **2000**, *104*, 794−800.
(56) Kundu, S.; Rane, V. Design and Photo-Induced Dynamics of Radical-Chromophore Adducts with One- or Two-Atom Separation: Toward Potential Probes for High Field Optical DNP Experiments. *J. Phys. Chem. B* **2020**, *124*, 3163−3179.
(57) Percival, P. W.; Hyde, J. S. Pulsed EPR Spectrometer, II. *Rev. Sci. Instrum.* **1975**, *46*, 1522−1529.
(58) Misra, S. K. *Handbook of Multifrequency Electron Paramagnetic Resonance: Data and Techniques*; John Wiley & Sons, Inc., 2014; pp 1−302.
(59) Blank, A.; Halevy, R.; Shklyar, M.; Shtirberg, L.; Kuppusamy, P. ESR Micro-Imaging of LiNc-BuO Crystals in PDMS: Spatial and Spectral Grain Distribution. *J. Magn. Reson.* **2010**, *203*, 150−155.
(60) Twig, Y.; Dikarov, E.; Hutchison, W. D.; Blank, A. Note: High Sensitivity Pulsed Electron Spin Resonance Spectroscopy with Induction Detection. *Rev. Sci. Instrum.* **2011**, *82*, No. 076105.
(61) Dayan, N.; Ishay, Y.; Artzi, Y.; Cristea, D.; Reijerse, E.; Kuppusamy, P.; Blank, A. Advanced Surface Resonators for Electron Spin Resonance of Single Microcrystals. *Rev. Sci. Instrum.* **2018**, *89*, No. 124707.
(62) Narkowicz, R.; Suter, D.; Stonies, R. Planar Microresonators for EPR Experiments. *J. Magn. Reson.* **2005**, *175*, 275−284.
(63) Xu, L.; Zhang, J.; Yin, L.; Long, X.; Zhang, W.; Zhang, Q. Recent Progress in Efficient Organic Two-Photon Dyes for Fluorescence Imaging and Photodynamic Therapy. *J. Mater. Chem. C* **2020**, *8*, 6342−6349.
(64) Albota, M.; Beljonne, D.; Brédas, J.; Ehrlich, J. E.; Heikal, A. A.; Hess, S. E.; Kogej, T.; Levin, M. D.; Marder, S. R.; Mccord-maughon, D.; Perry, J. W.; Röckel, H.; Rumi, M.; Webb, W. W.; Wu, X.; Xu, C.; Albota, M.; Beljonne, D.; Ehrlich, J. E.; Fu, J.; Heikal, A. A.; Hess, S. E.; Mccord-maughon, D.; Perry, J. W.; Rockel, H.; Rumi, M.; Subramaniam, G.; Webb, W. W. Design of Organic Molecules with Large Two-Photon Absorption Cross Sections Published by: American Association for the Advancement of Science Stable URL: Design of Organic Molecules with Large Two-Photon Absorption Cross Sections. *Science* **1998**, *281*, 1653−1656.
(65) Ricard, C.; Arroyo, E. D.; He, C. X.; Portera-Cailliau, C.; Lepousez, G.; Canepari, M.; Fiole, D. *Two-Photon Probes for In Vivo Multicolor Microscopy of the Structure and Signals of Brain Cells*; Springer: Berlin, 2018; Vol. *223*.
(66) Bolze, F.; Jenni, S.; Sour, A.; Heitz, V. Molecular Photosensitisers for Two-Photon Photodynamic Therapy. *Chem. Commun.* **2017**, *53*, 12857−12877.
(67) Multiphoton Absorption Spectra|KBFI. https://kbfi.ee/chemical-physics/research/nonlinear-spectroscopy/multiphoton-spectra/?lang=en (accessed Nov 12, 2021).
(68) Melnikov, A. S.; Serdobintsev, P. Y.; Vedyaykin, A. D.; Khodorkovskii, M. A. Two-Photon Absorption Cross Section for Coumarins 102, 153 and 307. *J. Phys. Conf. Ser.* **2017**, *917*, No. 062029.
(69) Bergman, A.; Jortner, J. Two-Photon Spectroscopy Utilizing Dye Lasers. *Chem. Phys. Lett.* **1972**, *15*, 309−315.
(70) Homans, R. J.; Khan, R. U.; Andrews, M. B.; Kjeldsen, A. E.; Natrajan, L. S.; Marsden, S.; McKenzie, E. A.; Christie, J. M.; Jones, A. R. Two Photon Spectroscopy and Microscopy of the Fluorescent Flavoprotein, ILOV. *Phys. Chem. Chem. Phys.* **2018**, *20*, 16949−16955.

(71) Birge, R. R. One-Photon and Two-Photon Excitation Spectroscopy.*Ultrasensitive Laser Spectroscopy*; Academic Press, Inc., 1983.
(72) König, K. Cell Damage During Multi-Photon Microscopy. *Handbook of Biological Confocal Microscopy*; Springer, 2006; Vol. *259*, pp 680−689.
(73) König, K.; Riemann, I.; Fischer, P.; Halbhuber, K. J. Multiplex FISH and Three-Dimensional DNA Imaging with near Infrared Femtosecond Laser Pulses. *Histochem. Cell Biol.* **2000**, *114*, 337−345.
(74) Redlich, M. J.; Prall, B.; Canto-Said, E.; Busarov, Y.; Shirinyan-Tuka, L.; Meah, A.; Lim, H. High-Pulse-Energy Multiphoton Imaging of Neurons and Oligodendrocytes in Deep Murine Brain with a Fiber Laser. *Sci. Rep.* **2021**, *11*, No. 7950.
(75) Botchway, S. W.; Charnley, M.; Haycock, J. W.; Parker, A. W.; Rochester, D. L.; Weinstein, J. A.; Williams, J. A. G. Time-Resolved and Two-Photon Emission Imaging Microscopy of Live Cells with Inert Platinum Complexes. *Proc. Natl. Acad. Sci. U.S.A.* **2008**, *105*, 16071−16076.
(76) Baggaley, E.; Botchway, S. W.; Haycock, J. W.; Morris, H.; Sazanovich, I. V.; Williams, J. A. G.; Weinstein, J. A. Long-Lived Metal Complexes Open up Microsecond Lifetime Imaging Microscopy under Multiphoton Excitation: From FLIM to PLIM and Beyond. *Chem. Sci.* **2014**, *5*, 879−886.
(77) Macias-Romero, C.; Zubkovs, V.; Wang, S.; Roke, S. Wide-Field Medium-Repetition-Rate Multiphoton Microscopy Reduces Photodamage of Living Cells. *Biomed. Opt. Express* **2016**, *7*, 1458.
(78) Hasan, M. T.; Theer, P.; Denk, W. Two-Photon Imaging to a Depth of 1000 Mm in Living Brains by Use of a Ti:Al_2O_3 Regenerative Amplifier. *Opt. Lett.* **2003**, *28*, 1022−1024.
(79) Twig, Y.; Dikarov, E.; Hutchison, W. D.; Blank, A. High Sensitivity Pulsed Electron Spin Resonance Spectroscopy with Induction Detection. *Rev. Sci. Instrum.* **2011**, *82*, No. 076105.
(80) Karpf, S.; Riche, C. T.; Di Carlo, D.; Goel, A.; Zeiger, W. A.; Suresh, A.; Portera-Cailliau, C.; Jalali, B. Spectro-Temporal Encoded Multiphoton Microscopy and Fluorescence Lifetime Imaging at Kilohertz Frame-Rates. *Nat. Commun.* **2020**, *11*, No. 2062.
(81) Samuni, A.; Carmichael, A. J.; Russo, A.; Mitchell, J. B.; Riesz, P. On the Spin Trapping and ESR Detection of Oxygen-Derived Radicals Generated inside Cells. *Proc. Natl. Acad. Sci. U.S.A.* **1986**, *83*, 7593−7597.
(82) Finikova, O. S.; Lebedev, A. Y.; Aprelev, A.; Troxler, T.; Gao, F.; Garnacho, C.; Muro, S.; Hochstrasser, R. M.; Vinogradov, S. A. Oxygen Microscopy by Two-Photon-Excited Phosphorescence. *ChemPhysChem* **2008**, *9*, 1673−1679.
(83) Sakadžić, S.; Roussakis, E.; Yaseen, M. A.; Mandeville, E. T.; Srinivasan, V. J.; Arai, K.; Ruvinskaya, S.; Devor, A.; Lo, E. H.; Vinogradov, S. A.; Boas, D. A. Two-Photon High-Resolution Measurement of Partial Pressure of Oxygen in Cerebral Vasculature and Tissue. *Nat. Methods* **2010**, *7*, 755−759.
(84) Subramanian, S.; Matsumoto, K. I.; Mitchell, J. B.; Krishna, M. C. Radio Frequency Continuous-Wave and Time-Domain EPR Imaging and Overhauser-Enhanced Magnetic Resonance Imaging of Small Animals: Instrumental Developments and Comparison of Relative Merits for Functional Imaging. *NMR Biomed.* **2004**, *17*, 263−294.
(85) Eaton, G. R.; Eaton, S. S. Introduction to EPR Imaging Using Magnetic-Field Gradients. *Concepts Magn. Reson.* **1995**, *7*, 49−67.
(86) Rugar, D.; Yannoni, C. S.; Sidles, J. A. Mechanical Detection of Magnetic Resonance. *Nature* **1992**, *360*, 563−566.
(87) Durkan, C.; Welland, M. E. Electronic Spin Detection in Molecules Using Scanning-Tunneling- Microscopy-Assisted Electron-Spin Resonance. *Appl. Phys. Lett.* **2002**, *80*, 458−460.
(88) Le Sage, D.; Arai, K.; Glenn, D. R.; Devience, S. J.; Pham, L. M.; Rahn-Lee, L.; Lukin, M. D.; Yacoby, A.; Komeili, A.; Walsworth, R. L. Optical Magnetic Imaging of Living Cells. *Nature* **2013**, *496*, 486−489.
(89) Sushkov, A. O.; Chisholm, N.; Lovchinsky, I.; Kubo, M.; Lo, P. K.; Bennett, S. D.; Hunger, D.; Akimov, A.; Walsworth, R. L.; Park, H.; Lukin, M. D. All-Optical Sensing of a Single-Molecule Electron Spin. *Nano Lett.* **2014**, *14*, 6443−6448.
(90) Shi, F.; Kong, F.; Zhao, P.; Zhang, X.; Chen, M.; Chen, S.; Zhang, Q.; Wang, M.; Ye, X.; Wang, Z.; Qin, Z.; Rong, X.; Su, J.; Wang, P.; Qin, P. Z.; Du, J. Single-DNA Electron Spin Resonance Spectroscopy in Aqueous Solutions. *Nat. Methods* **2018**, *15*, 697−699.
(91) Lurie, D. J.; Li, H.; Petryakov, S.; Zweier, J. L. Development of a PEDRI Free-Radical Imager Using a 0.38 T Clinical MRI System. *Magn. Reson. Med.* **2002**, *47*, 181−186.
(92) Krainz, T.; Gaschler, M. M.; Lim, C.; Sacher, J. R.; Stockwell, B. R.; Wipf, P. A Mitochondrial-Targeted Nitroxide Is a Potent Inhibitor of Ferroptosis. *ACS Cent. Sci.* **2016**, *2*, 653−659.
(93) Sun, J.; Wang, S.; Bu, W.; Wei, M. Y.; Li, W. W.; Yao, M. N.; Ma, Z. Y.; Lu, C. T.; Li, H. H.; Hu, N. P.; Zhang, E. H.; Yang, G. D.; Wen, A. D.; Zhu, X. H. Synthesis of a Novel Adamantyl Nitroxide Derivative with Potent Anti-Hepatoma Activity in Vitro and in Vivo. *Am. J. Cancer Res.* **2016**, *6*, 1271−1286.
(94) Yang, L.; Wang, M. J.; Zhang, Z. J.; Morris-Natschke, S. L.; Goto, M.; Tian, J.; Liu, Y. Q.; Wang, C. Y.; Tian, X.; Yang, X. M.; Lee, K. H. Synthesis of Novel Spin-Labeled Derivatives of 5-FU as Potential Antineoplastic Agents. *Med. Chem. Res.* **2014**, *23*, 3269−3273.
(95) Ye, S.; Xu, P.; Huang, M.; Chen, X.; Zeng, S.; Wang, Q.; Chen, J.; Li, K.; Gao, W.; Liu, R.; Liu, J.; Shao, Y.; Zhang, H.; Xu, Y.; Zhang, Q.; Zhong, Z.; Wei, Z.; Wang, J.; Hao, B.; Huang, W.; Liu, Q. The Heterocyclic Compound Tempol Inhibits the Growth of Cancer Cells by Interfering with Glutamine Metabolism. *Cell Death Dis.* **2020**, *11*, No. 312.
(96) Zhao, X. B.; Wu, D.; Wang, M. J.; Goto, M.; Morris-Natschke, S. L.; Liu, Y. Q.; Wu, X. B.; Song, Z. L.; Zhu, G. X.; Lee, K. H. Design and Synthesis of Novel Spin-Labeled Camptothecin Derivatives as Potent Cytotoxic Agents. *Bioorg. Med. Chem.* **2014**, *22*, 6453−6458.
(97) Ouari, O.; Polidori, A.; Pucci, B.; Tordo, P.; Chalier, F. Synthesis of a Glycolipidic Amphiphilic Nitrone as a New Spin Trap. *J. Org. Chem.* **1999**, *64*, 3554−3556.
(98) Shetty, S.; Kumar, R.; Bharati, S. Mito-TEMPO, a Mitochondria-Targeted Antioxidant, Prevents N-Nitrosodiethylamine-Induced Hepatocarcinogenesis in Mice. *Free Radical Biol. Med.* **2019**, *136*, 76−86.
(99) Gotham, J. P.; Li, R.; Tipple, T. E.; Lancaster, J. R.; Liu, T.; Li, Q. Quantitation of Spin Probe-Detectable Oxidants in Cells Using Electron Paramagnetic Resonance Spectroscopy: To Probe or to Trap? *Free Radical Biol. Med.* **2020**, *154*, 84−94.
(100) Janzen, E. G.; Lawrence, H. D.; Zhang, Y. K. Synthesis of a Novel Nitrone, 2-Phenyl-5, 5-Dimethyl-1-Pyrroline N-Oxide (Nitronyl-13C), for Enhanced Radical Addend Recognition and Spin Adduct Persistence. *J. Am. Chem. Soc.* **1994**, *116*, 3738−3743.
(101) Bacchiocchi, C.; Foschi, G.; Miglioli, I.; Shoarinejad, S.; Arcioni, A.; Zannoni, C. Nematic Director Configuration, Local Order and Microviscosity in a PSLC Cell. *Mol. Cryst. Liq. Cryst.* **2015**, *614*, 2−10.
(102) Siepe, S.; Herrmann, W.; Borchert, H. H.; Lueckel, B.; Kramer, A.; Ries, A.; Gurny, R. Microenvironmental PH and Microviscosity inside PH-Controlled Matrix Tablets: An EPR Imaging Study. *J. Controlled Release* **2006**, *112*, 72−78.
(103) Kempe, S.; Metz, H.; Mäder, K. Application of Electron Paramagnetic Resonance (EPR) Spectroscopy and Imaging in Drug Delivery Research - Chances and Challenges. *Eur. J. Pharm. Biopharm.* **2010**, *74*, 55−66.
(104) Komarov, D. A.; Ichikawa, Y.; Yamamoto, K.; Stewart, N. J.; Matsumoto, S.; Yasui, H.; Kirilyuk, I. A.; Khramtsov, V. V.; Inanami, O.; Hirata, H. In Vivo Extracellular PH Mapping of Tumors Using Electron Paramagnetic Resonance. *Anal. Chem.* **2018**, *90*, 13938−13945.
(105) Babić, N.; Peyrot, F. Molecular Probes for Evaluation of Oxidative Stress by In Vivo EPR Spectroscopy and Imaging: State-of-the-Art and Limitations. *Magnetochemistry* **2019**, *5*, No. 13.
(106) Kovaleva, E. G.; Molochnikov, L. S.; Venkatesan, U.; Marek, A.; Stepanova, D. P.; Kozhikhova, K. V.; Mironov, M. A.; Smirnov, A. I. Acid−Base Properties of Nanoconfined Volumes of Anodic Aluminum Oxide Pores by EPR of PH-Sensitive Spin Probes. *J. Phys. Chem. C* **2016**, *120*, 2703−2711.
(107) Kirk, M. L.; Shultz, D. A.; Hewitt, P.; Stasiw, D. E.; Chen, J.; van der Est, A. Chromophore-Radical Excited State Antiferromagnetic

https://doi.org/10.1021/acs.jpcb.1c10920
J. Phys. Chem. B 2022, 126, 2715−2728

Exchange Controls the Sign of Photoinduced Ground State Spin Polarization. *Chem. Sci.* **2021**, *12*, 13704−13710.
(108) Mayl, M.; Chen, S.; Lorenzo, E. R.; Wasielewski, M. R.; Richert, S. Exploring Photogenerated Molecular Quartet States as Spin Qubits and Qudits. *J. Am. Chem. Soc.* **2021**, 7050.
(109) In ref 42, there is an additional factor in the sensitivity expression for the number of hyperfine lines. It is not included in the current work, since in typical TREPR experiments only one hyperfine line is used for detection by fixing the Zeeman magnetic field at its resonance position.

https://doi.org/10.1021/acs.jpcb.1c10920
J. Phys. Chem. B 2022, 126, 2715−2728